Skyrmion States in Disk Geometry

Thomas Brian Winkler,[1,*] Kai Litzius,[2] Andrea de Lucia,[1] Markus Weißenhofer,[3] Hans Fangohr,[4,5,6,†] and Mathias Kläui[1,‡]

[1] *Institute of Physics, Johannes Gutenberg Universtät, Staudinger Weg 7, Mainz 55122, Germany*
[2] *Department of Materials Science and Engineering, Massachusetts Institute of Technology, Cambridge, Massachusetts 02142, USA*
[3] *Fachbereich Physik, Universität Konstanz, Universitätsstraße 10, Konstanz 78464, Germany*
[4] *Max-Planck Institute for Structure and Dynamics of Matter, Luruper Chaussee 149, Hamburg 22761, Germany*
[5] *European XFEL, Holzkoppel 4, Schenefeld 22869, Germany*
[6] *University of Southampton, Southampton SO17 1BJ, United Kingdom*

(Received 16 December 2020; revised 31 July 2021; accepted 22 September 2021; published 11 October 2021)

In this work, we explore the stability of magnetic skyrmions confined in a disk geometry by analyzing how to switch a skyrmionic state in a circular disk into a uniformly magnetized state when applying an external magnetic field. The technologically highly relevant energy barrier between the skyrmion state and the uniformly magnetized state is a key parameter needed for lifetime calculations. In an infinite sample, this relates to the out-of-plane *rupture field* against the skyrmion-core direction, while in confined geometries the topological charge can also be changed by interactions with the sample edges. We find that annihilating a skyrmion with an applied field in the direction of the core magnetization—we call this *expulsion*—the energy barrier to the uniform state is generally around one order of magnitude lower than the annihilation via the rupture of the core in the disk center, which is observed when the applied field is acting in the direction opposite to the core magnetization. For the latter case a Bloch point (BP) needs to be nucleated to change the topological charge to zero. We find that the former case can be realistically calculated using micromagnetic simulations but that the annihilation via rupture, involving a Bloch point, needs to be calculated with the Heisenberg model because the high magnetization gradients present during the annihilation process cannot be accurately described within the micromagnetic framework.

DOI: 10.1103/PhysRevApplied.16.044014

I. INTRODUCTION

Magnetic skyrmions [1,2] can be found in spin patterns of magnetic systems with broken inversion symmetry, e.g., in thin magnetic films with an interfacial Dzyaloshinskii-Moriya interaction (DMI) [3,4]. They are quasiparticles and their properties make them promising candidates for next-generation nonconventional computing and storage devices such as probabilistic computing [5,6] or race-track memory [7,8]. For such devices, controlled nucleation [9–11], annihilation [12], and movement [13,14] of skyrmions is generally required, while the existence or absence of a skyrmion defines the logical bit. Skyrmions can also be used in so-called bit-patterned media (BPM) [15], where magnetic disk structures in the nanometer range are lithographically patterned into a storage medium. In that way, the superparamagnetic limits of conventional magnetic storage devices can potentially be mitigated to some extent [16]. Apart from their potential for applications, skyrmions show interesting physical behavior, such as the skyrmion Hall angle [14,17]. Some of these effects may arise due to their quasiparticle nature and their topological stabilization. Recent work has shown pulse-induced nucleation of skyrmions or nucleation at pinning sites [9–11,18] but the nucleation process is still not well understood, since it is a process on and below the nanosecond time scale. However, nucleation of skyrmions is possible by applying in-plane (IP) fields, as shown in various experiments [18]. Likewise, the lifetime of skyrmions has been investigated [6,19] in the past, since this is an important parameter for device applications. However, the energy barrier between the skyrmionic and the uniformly magnetized state remains a mostly elusive, yet required, parameter for lifetime calculations and poses a major challenge for predicting the stability of skyrmions in potential new devices. In our setup, it is related to the annihilation field H^*, which is needed to transform the skyrmion state into the uniformly magnetized state via an out-of-plane

*twinkler@uni-mainz.de
†hans.fangohr@mpsd.mpg.de
‡Klaeui@uni-mainz.de

(OOP) field. The field is applied in both directions; in the skyrmion-core direction and against the skyrmion core. The lifetime also depends on the temperature and the attempt frequency, according to the Arrhenius-Neél law [12,20,21]. To model future devices effectively, it is important to know how a magnetic system will behave under certain conditions and how magnetic parameters influence this behavior. This approach is important to avoid inefficient "trial-and-error" fabrications. Furthermore, the energy barrier of skyrmionic states is of interest to understand the physics of topological protected spin structures and how much their topology can contribute to their enhanced stability. Moreover, it is important to know the limitations of a chosen simulation model.

In this work, we investigate the dependence of H^* on all key magnetic material parameters, namely the exchange constant, the DMI strength, the anisotropy constant, and the saturation magnetization. We vary the disk size to analyze the dependence of the annihilation field on the geometry present and we ascertain the computational models required for robust analysis of the value of the annihilation field. Using a multiscale model, we demonstrate where the Heisenberg (HB) model is required and where conventional micromagnetic approaches are sufficient.

II. COMPUTATIONAL MODELS

We use two different computational methods to simulate the physics of the system: the micromagnetic model (MM), which assumes that the magnetization of the sample is a vector field defined on a continuous region in space, and a Heisenberg model, which represents the individual magnetic moments of individual atoms.

A. Micromagnetics

The MM model [22] describes the magnetization using partial differential equations (PDEs) derived from classical field theory. While these PDEs have to be discretized and solved numerically, we can choose a discretization cell size that is significantly larger than the spacing of the actual magnetic moments. For this reason, one is able to simulate the behavior of experimentally relevant mesoscopic samples. The MM approach is generally not valid when the system shows strong spatial variations of the spin texture. This is the case for small skyrmions or when dynamic processes involving Bloch-point (BP)-type [23] configurations occur. Then, the spatial derivative of the MM magnetization function can diverge: it is an assumption of the numerical micromagnetic model that the magnetization vector field changes slowly as a function of space [22]. For example, it has been shown that the micromagnetic exchange energy significantly overestimates the exchange energy of a spin-wave system with a wavelength of the order of the cell size [24].

B. Heisenberg model

The HB model [25] represents the magnetization through dipole moments that are associated with the discrete magnetic moments in the crystal lattice. It is a more accurate way of the sample than the micromagnetic model: we can simulate every single magnetic moment and the HB model makes no approximations regarding the spatial variation in the magnetic moments.

However, due to the larger computational cost, the material volume that can be simulated in the HB model is limited [26].

C. Hamiltonians

We next describe the Hamiltonians for the discretized MM model and the HB model.

The exchange-energy values E_{xc} for the Hamiltonian for the HB and the MM model are given by

$$E_{\mathrm{xc,HB}} = -\frac{1}{2}\sum_{i,j} J_{i,j}\,\mathbf{S}_i \cdot \mathbf{S}_j\,, \tag{1}$$

$$E_{\mathrm{xc,MM}} = \frac{A}{M_s^2}\int_V dr|\nabla \mathbf{M}(\mathbf{r})|^2, \tag{2}$$

where $\mathbf{S}_i$ the spin vector at position $\mathbf{r}_i$, and $|\mathbf{S}_i| = \mu_i$ is its magnetic moment, and $J_{i,j}$ is the exchange coupling constant between spin i and spin j. In the MM model, $\mathbf{M}(\mathbf{r})$ is the magnetization at point $\mathbf{r}$ with the saturation magnetization $M_S = |\mathbf{M}|$ and A the exchange stiffness.

The conversion between the models can be realized using $\mu = a^3 M_S$ and $A = J \cdot \mathbf{S}^2 \cdot c_s/a$, where a is the lattice constant and c_s is the number of nearest neighbors in the lattice [27]. To describe the Dzyaloshinskii-Moriya interaction (DMI), the energy terms in the two models are as follows:

$$E_{\mathrm{DMI,HB}} = \frac{1}{2}\sum_{i,j} \mathbf{D}_{i,j} \cdot \mathbf{S}_i \times \mathbf{S}_j\,, \tag{3}$$

$$E_{\mathrm{DMI,MM}} = \frac{A}{M_S^2}\int_V dV D_a \mathbf{M}(\mathbf{r}) \cdot [\nabla \times \mathbf{M}(\mathbf{r})], \tag{4}$$

where D is the DMI interaction strength, $\mathbf{D} = D\mathbf{r}_{i,j} \times \mathbf{e}_z$ for interfacial DMI, and $D_a = -D/a^2$, where $r_{i,j}$ is the distance between two neighboring spins and e_z is the unit vector in the z direction. For Zeeman and the uniaxial anisotropy energy, the terms for HB and a discretized MM model are equivalent; hence we provide only the HB description:

$$E_{\mathrm{Zeeman}} = -\mu_0 \sum_i \mathbf{H}_{\mathrm{ext}} \cdot \mathbf{S}_i, \tag{5}$$

$$E_{\mathrm{Anisotropy}} = -\mu_0 \sum_i K_u \cdot (\mathbf{S}_i \cdot \mathbf{e}_u)^2, \tag{6}$$

where $\mathbf{H}_{\text{ext}}$ is the external field, K_u is the anisotropy constant, and $\mathbf{e}_u$ is the unit vector in direction of the low-energy axis. The MM expression can be obtained by substituting $\mathbf{S}$ with the MM magnetization vector $\mathbf{M}$.

The dipolar energy relates to the stray field and can be computed as the sum over all dipole-dipole interactions between two spins. The energy contribution of a magnetic dipole μ_2 exposed to the stray field $H_{\mu 1}$ of dipole μ_1 in the Heisenberg model is

$$E_{\text{Zeeman}} = -\mu_2 \cdot \mathbf{H}_{\mu_1} = \frac{\mu_0}{4\pi}\left(\frac{\mu_1 \cdot \mu_2}{r^3} - 3\frac{(\mathbf{r}\cdot\mu_1)(\mathbf{r}\cdot\mu_2)}{r^5}\right), \tag{7}$$

where $\mathbf{r}$ is the distance of the evaluated spin pair.

The computational effort of the total energy of the system is of complexity $\mathcal{O}(N^2)$, where N is the number of spins, due to its pairwise nature. For the micromagnetic model, the structure and computational complexity of the equation for conventional calculations is similar and N represents the number of discretization cells.

A more efficient way of solving this convolution operation is to carry it out in Fourier space [28]. Both the MM and the HB model use a demagnetization tensor combined with a fast Fourier transform (FFT) to calculate the stray field efficiently. While the MM framework uses the demagnetization tensor according to the calculations by Newell *et al.* [29], the demagnetization tensor $\underline{N}_{\text{HB}}$ of the HB model is calculated as [24]

$$\underline{N}_{\text{HB}} = \frac{1}{4\pi}\left[\frac{\mathbb{1}}{|\mathbf{r_i}-\mathbf{r_j}|^3} - 3\frac{(\mathbf{r_i}-\mathbf{r_j})\bigotimes(\mathbf{r_i}-\mathbf{r_j})}{|\mathbf{r_i}-\mathbf{r_j}|^5}\right]. \tag{8}$$

For the MM simulations, the graphics-processing-unit- (GPU) enabled software package MicroMagnum [30,31] is used, with extensions for DMI [32]. The HB code is adapted from MicroMagnum, validated in Ref. [24], and it has recently been parallelized for a GPU [33].

D. Multiscale model

To combine the advantages of the MM and HB simulation models, a multiscale (MS) MicroMagnum approach is used [24,33], with DMI included. The central idea is to use a micromagnetic model where possible and to use the—more accurate and computationally more expensive—HB model where necessary. A schematic illustration of the idea is shown in Fig. 1(b). The MS simulation approach is an efficient method to simulate next-generation devices, since large mesoscopic samples have to be simulated micromagnetically, while HB model accuracy may be necessary for accurate dynamics of the system on atomistic length scales. Both solvers are connected with cross-scale effective field terms for the nearest-neighbor interactions as well as for the stray field, which yield a correct transition of the two solver regions. For more details about the embedding and verification of the HB solver into the MM

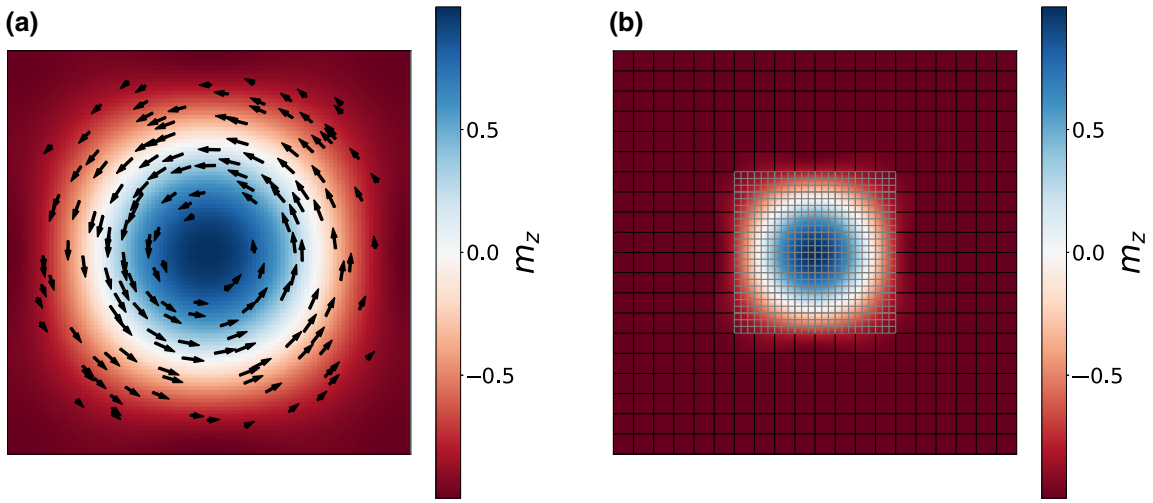

FIG. 1. (a) An illustration of a Bloch-skyrmion configuration computation using the micromagnetic model (the pure HB and the multiscale models produce very similar results). The arrows and their size indicate the direction and strength of the in-plane component, while the color indicates the out-of-plane magnetization component. The skyrmion core (blue) is pointing into the plane, whereas the surroundings point out of the plane. In the remainder of this work, we study such Bloch skyrmions confined in a cylindrical disklike geometry. The size of a typical skyrmion can reach from a few nanometers up to a few micrometers. (b) The concept of the multiscale approach [24]: a part of the simulation (here shown with the gray mesh) can be computed atomistically, whereas all other parts are computed using the micromagnetic model. A typical application is to use an atomistic region (such as here the skyrmion) for the part of the sample that shows high spin canting and in which the micromagnetic assumption may break down and to use a micromagnetic model for those parts of the sample where the magnetization gradient is lower (such as the nearly homogeneous magnetization surrounding the skyrmion in this pedagogical example).

mesh and the time integration, see Ref. [24]. Our investigation shows in which cases of the skyrmion annihilation a MM simulation is suitable and when a more accurate HB model is necessary.

E. Torque minimization

Our expanded MicroMagnum software package (as outlined above) performs micromagnetic and HB simulations on a rectilinear spatial grid. For the relaxation of initial states and the determination of (meta)stable configurations, we use the dissipative Landau-Lifshitz-Gilbert (LLG) equation [34] to find the steepest gradient energy path, which is given by only the dissipative term of the Landau-Lifshitz equation:

$$\frac{d\mathbf{m}}{dt} = -\alpha\gamma\,\mathbf{m}\times\mathbf{m}\times\mathbf{H}^{\text{eff}}, \tag{9}$$

where $\mathbf{m}$ refers to our (macro)spin in the respective simulation model (i.e., in the Heisenberg model, it is the atomistic magnetic moment with $\mathbf{m}\mu = \mathbf{S}$, and in the micromagnetic model, it is the magnetic moment associated with a uniformly magnetized micromagnetic discretization cell, with $\mathbf{m}\cdot M_S = \mathbf{M}$), α is the damping constant, γ is the gyromagnetic ratio, and $\mathbf{H}^{\text{eff}}$ the effective field acting on the spin, containing all energy contributions. It is possible to neglect the precession term in the Landau-Lifshitz-Gilbert equation here, since we are not interested in the correct precessional dynamics but only in the relaxed state, i.e., we use the dissipative equation to minimize the energy of the system. The damping constant is chosen to be $\alpha = 0.5$ to accelerate the process of finding the nearest (meta)stable configuration.

III. SIMULATION PROTOCOL

The investigated system is a circular disk with diameter $d = 160$ nm and thickness $t = 4.8$ nm. The lattice constant a of the HB model is chosen as $a = 0.4$ nm in each direction. For the micromagnetic regions in the MS approach, the cell size is chosen as $\Delta x = \Delta y = 2$ nm, while the cell size in the z direction is as thick as the sample, $\Delta z = t = 4.8$ nm, which is a size comparable to the effective thickness of thin-film systems [13]. The circular shape of the disk is chosen to address the shape of the skyrmion and to avoid deformations due to the geometry. We use interfacial DMI, as it is present in thin-film systems with broken inversion symmetry [35].

To determine the skyrmion states, simulations are performed with the following protocol. A skyrmion is artificially put into the system by initializing a uniform state pointing in the z direction out of the plane, with a centered circular area magnetized in the opposite direction. The radius of this area is chosen with 40 nm. Then this initial state is relaxed to ensure that we have at least a skyrmion state as a (meta)stable state for different values of the material parameters M_S, A, D, and K_u. The relaxation occurs via torque minimization by time integration of the dissipative LLG equation. Figure 2(d) shows such a configuration and we discuss the observed initial configurations systematically in Sec. A and Fig. 3.

Those parameter combinations that exhibit a skyrmion after energy minimization are used for further investigations: we apply out-of-plane fields until the skyrmion is annihilated at an annihilation field H^*, which we aim to determine.

In more detail, the annihilation field H^* is determined by applying an external magnetic OOP field either in the direction of the skyrmion-core magnetization or in the opposite direction to the skyrmion-core magnetization.

The field is increased in steps with an adjustable step size and a subsequent relaxation, i.e., energy minimization. The simulation starts with large field steps. When the skyrmion annihilates, the last stable skyrmion configuration is reloaded and the field step is then decreased. The process is repeated consecutively with smaller field steps until the desired accuracy of 1 mT in the applied field is reached. More precisely, the field steps are adjusted logarithmically (1000 mT, 100 mT, 10 mT, 1 mT). It is important to not choose too large instantaneous jumps of the field; otherwise, an overshooting of the skyrmion during the shrinking process can annihilate it prematurely due to the excited dynamics [36].

For the MS model approach, the simulation is started with just one MM region. The HB solver is added to the simulation, when the skyrmion is small enough to fit into the 40 nm × 40 nm area, which is the size of the HB solver in the MM simulation. For more details about the implementation and validation of the MS approach, see Ref. [24]. Purely HB model and purely MM simulations are performed in the same way for validation and comparison, respectively.

In the case of the applied field acting in the direction of the skyrmion core, we observe an expansion of the skyrmion core and an unwinding of the magnetization helix at the open boundary of the sample. In this scenario, we call the annihilation field the *expulsion* field $H_{\text{exp}} = H^*$. The process can be seen in Figs. 2(d)–2(f) and is discussed in detail in Sec. D. In the expulsion case, we fix the field step directly at 1 mT, since the relaxation of the increasing skyrmion at larger steps takes more computation time than a larger number of relaxations at smaller field steps.

In the case of the applied field acting in the direction opposite to the magnetization in the skyrmion core, we observe shrinking of the skyrmion core until the skyrmion disappears. In this scenario, we call the annihilation field the *rupture* field $H_{\text{rup}} = H^*$. The process can be seen in Figs. 2(a)–2(d) and is discussed in detail in Sec. B.

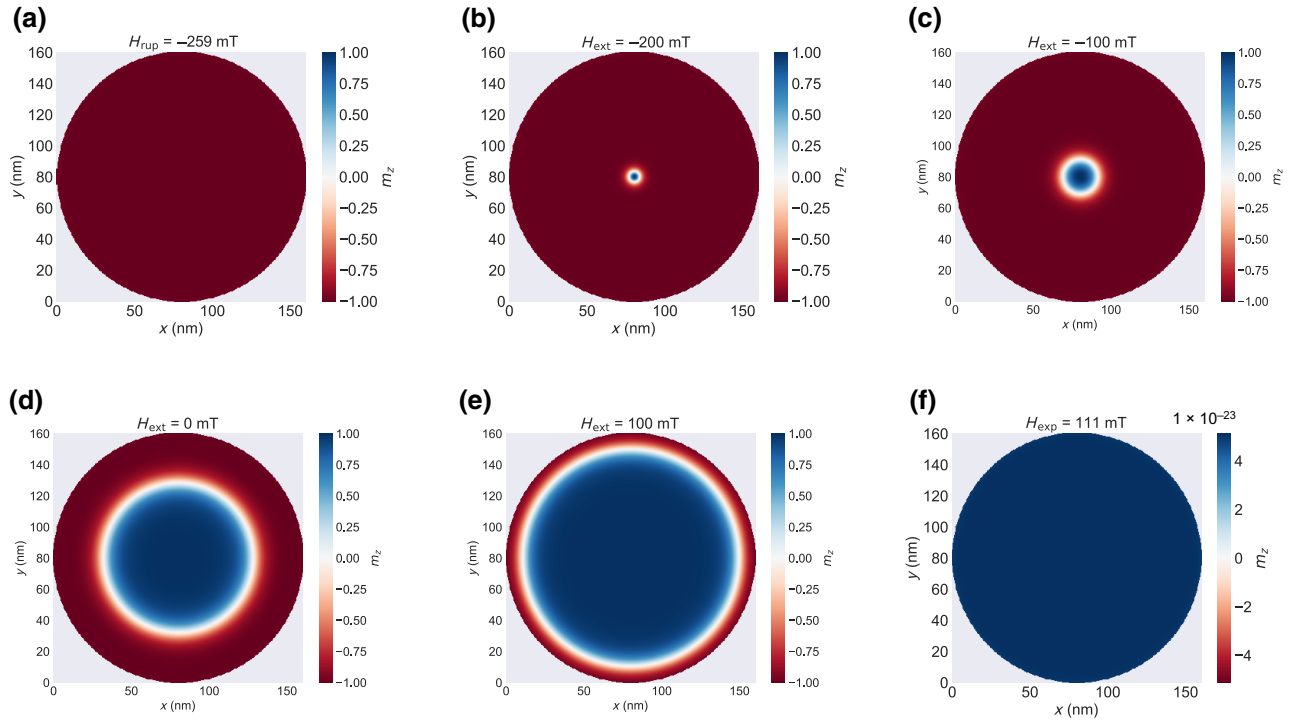

FIG. 2. The process of rupture and expulsion of a skyrmion, starting at zero field (d). Applying the field against the skyrmion core [(b),(c)], its center shrinks until a BP ruptures the topological charge [the process is visualized in Fig. 6(a)] and the system stays in the uniform state (a). Applying the field in skyrmion-core direction, it blows up (e) until the topological charge is eliminated at the sample boundaries, also ending up in a uniform state (f). Once the skyrmion is annihilated, it is not possible to reverse the process with an applied field alone.

Regarding the computational models, we run simulations using the micromagnetic model (as it is the fastest) or the multiscale model if required. We carry out regular simulations with the full HB model (with the assumption that this provides the most accurate numerical solution) to ensure that the results of the other computational models are accurate.

While they are discussed in more detail in the following sections, we can summarize the key findings already here for guidance. The expulsion process can be accurately simulated using the micromagnetic model. For the rupture process, the skyrmion shrinks and collapses when it reaches H_{rup}. At that point, the simulation grid is no longer able to resolve the skyrmion size. We find that this process needs to be resolved atomistically (Sec. C), so that we need to use the multiscale model with a Heisenberg model around the collapsing skyrmion (or use the—computationally more expensive—Heisenberg model for the whole sample).

IV. RESULTS

A. Initial configuration

We follow the procedure described in Sec. III to establish an initial magnetic configuration for each combination of four material parameters. We vary the material parameters, such as the saturation magnetization M_s, the anisotropy strength K_u, the exchange coupling A, and the DMI strength D, systematically.

Figure 3 shows such initial configurations obtained for selected parameter combinations. For all of them, there is no external field applied and they have been calculated in a micromagnetic model with a discretization cell with edge lengths of 2 nm in the x direction and 2 nm in the y direction (the two lateral dimensions) and one cell in the z direction with edge length $\Delta_z = t = 4.8$ nm. A finer discretization of the disk in the z direction may change the configuration [37] but several data points are repeated using the full Heisenberg model and all reported states are also metastable in the Heisenberg model.

We observe different classes of configurations in Fig. 3, including a skyrmion [e.g., the middle row in Fig. 3(b) for $D \geq 1.2$ mJ/m^2], a uniform state [for example, the left row in Fig. 3(b) for $K_u \geq 120$ MJ/m^3], and targetlike configurations in the bottom-right corner of Fig. 3(b), which have also been reported in Ref. [37]. Deformed topological objects are also visible—e.g., in the top-right corner of Fig. 3(d)—which carry a topological charge of 1 but do not show a circular shape after the initialization. In Fig. 3(e), the three top configurations in the right corner are so-called incomplete skyrmions, with a topological charge below 1 [37]. We also see two states that undergo a BP reversal, which results from zero anisotropy [e.g., in

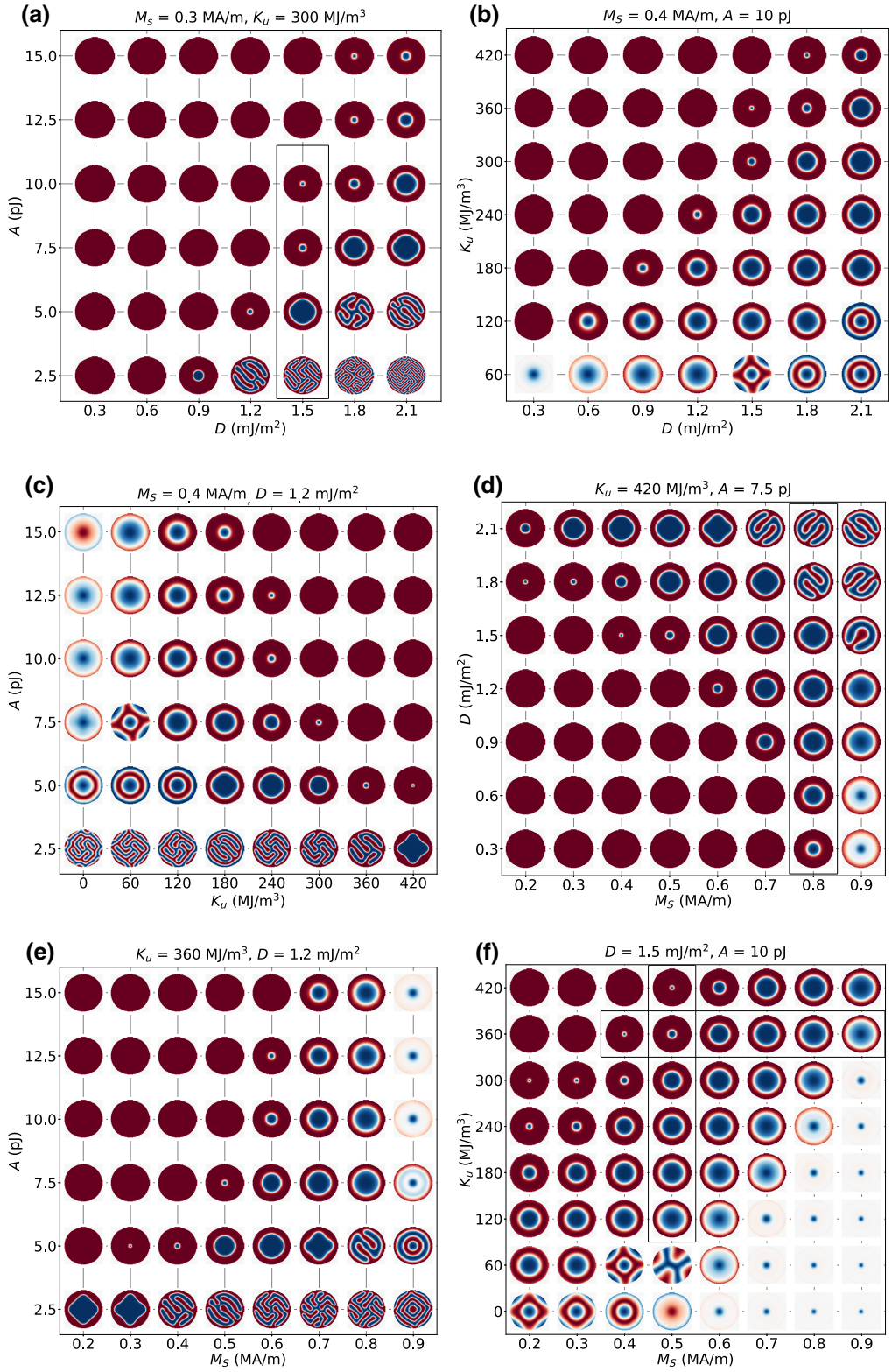

FIG. 3. Metastable configurations at zero field for selected magnetic material parameter combinations. The colors indicate the normalized out-of-plane magnetization component (blue = −1, red = 1, white = 0). Six two-dimensional cuts through the phase space are shown. The configuration in each circle shows the metastable states after relaxation of an initial skyrmion on the 160-nm disk. Configurations enclosed by a black box indicate configuration sets that are analyzed in more detail in the following sections.

Fig. 3(c), the top-left configuration]. Further, spin spiral states are visible [the bottom-right corner of Fig. 3(a)].

It is visible from Fig. 3(a) that skyrmions exist within a certain range of the DMI strength D and the exchange constant A. For large values of D, the system relaxes into a spin spiral state, whereas large values of A favor the uniform state (US). Thus, neglecting other effects, skyrmions exist for a distinct ratio A/D. Due to similar effects of A and K_u, the skyrmion states show a band shape in the respective plot, where both values cannot be too high or low [see Fig. 3(c)]. However, low exchange prefers spin spiral states, while low anisotropy favors targetlike states, as is visible in Figs. 3(b), 3(c), and 3(f). These findings about the skyrmionic phase are in good agreement with the literature [19,37,38], where skyrmions are at least metastable when the magnetic parameter configuration does not differ from the ratio of D/D_c to a great extent, with the critical DMI $D_c = \sqrt{\mathrm{AK}}/\pi$. Since we have OOP anisotropy, the effect of increasing K_u is similar to increasing the exchange [Fig. 3(b)]. Varying M_S, one sees a transition from the uniform to the skyrmion phase and then into an in-plane configuration above the spin-reorientation transition [Figs. 3(d), 3(e), and 3(f)] [39]. This happens due to the strong far field, which is generated by the OOP magnetization. Lower anisotropy makes the IP skyrmion domain wall (DW) energetically more favorable and can stabilize them in a low-K_u and low-M_S system [Fig. 3(f), for $M_S = 0.7$ MA/m. The DW width increases with lower K_u] by reducing surface charges. In an intermediate range of dipolar interactions, skyrmions can occur due to stray-field stabilization, reducing the far field of the sample. This result is also in agreement with the literature [19,40].

B. Rupture field of skyrmions

Starting from the initial skyrmion states obtained at zero applied field (see Sec. A), we now investigate the process of annihilating the skyrmion by applying an external field. In particular, given the initial skyrmion configuration as represented in Fig. 2(d), we apply an external field in the negative z direction. The skyrmion core will shrink [Fig. 2(c)] in response to this, to reduce the Zeeman energy in the core area (where the applied field points in the opposite direction to the magnetization field in the core). As the field is increased further, the skyrmion shrinks further [Fig. 2(b)] and at some point disappears, leading to the configuration shown in Fig. 2(a).

Figure 4 shows the annihilation process in more detail. We show a cross-section side view of the disk, focused at the skyrmion core in the configuration where the skyrmion core has shrunk to its smallest possible size. This is a the situation between Figs. 2(b) and 2(a). The blue vertical region in Fig. 4(a) is the skyrmion core and the color represents the z component of the magnetization, which is pointing in the $+z$ direction in the skyrmion core. The external field is acting in the opposite direction ($-z$).

These simulation results are obtained using the Heisenberg model with a 0.4 nm spacing between the magnetic moments. As the thickness of the sample is 4.8 nm, we have 12 discrete layers in the z direction in the HB model. The numbers on the y axes of the subplots correspond to these layers.

Figures 4(a)–4(i) represent different times in the magnetization dynamics that is computed for the annihilation of the skyrmion. In Figs. 4(d), 4(e), and 4(f), we can see a reversal of the magnetization, starting from the bottom and propagating toward the top of the sample. The reversal of the skyrmion core is completed in Fig. 4(i).

We interpret the data in Figs. 4(d)–4(f) as a Bloch point [23] entering the sample at the bottom and moving up along the skyrmion core to the top of the sample, thereby facilitating the reversal [37] of the magnetization. From a topological perspective—where we assume that the magnetization vector field is continuous—the skyrmion can only disappear from the sample by breaking that continuity, i.e., by creating a (topological) rupture in the field. This is the reason for describing this annihilation process as the rupture and the associated applied field at which this annihilation occurs as the *rupture field* H_{rup} and also highlights the importance of the MS model, since these dynamics cannot be resolved in the MM model. For nonskyrmion configurations, we define H_{rup} as the field where the magnetization makes its transition to the uniformly magnetized phase.

We compute this rupture field systematically for those material parameter combinations shown in Fig. 3, following the iterative incrementing of the applied field as described in III.

Figure 5 shows the rupture field as a function of one material parameter per subplot for a subset of all combinations. Figure 9 in the Appendix shows the rupture field for all the configurations shown in Fig. 3.

Figure 5(a) shows the rupture field H_{rup} as a function of the exchange stiffness A, where H_{rup} decreases with increasing A. A strong exchange constant A favors the uniform configuration, since the exchange energy is minimized for a parallel alignment of the spins in a ferromagnet. We can also look at the energy of a (skyrmion) domain wall, for which the energy density is given by [41]

$$\sigma_{\mathrm{DW}} \propto 4\sqrt{\mathrm{AK}} - \pi |D|. \tag{10}$$

The energy of the skyrmion will thus increase for increasing A mainly due to the spin canting in the DW. Thus, the presence of DWs becomes energetically unfavorable with increasing A, increasing the energy level for the skyrmion and in this case consequently lowering the energy barrier toward the uniform configuration.

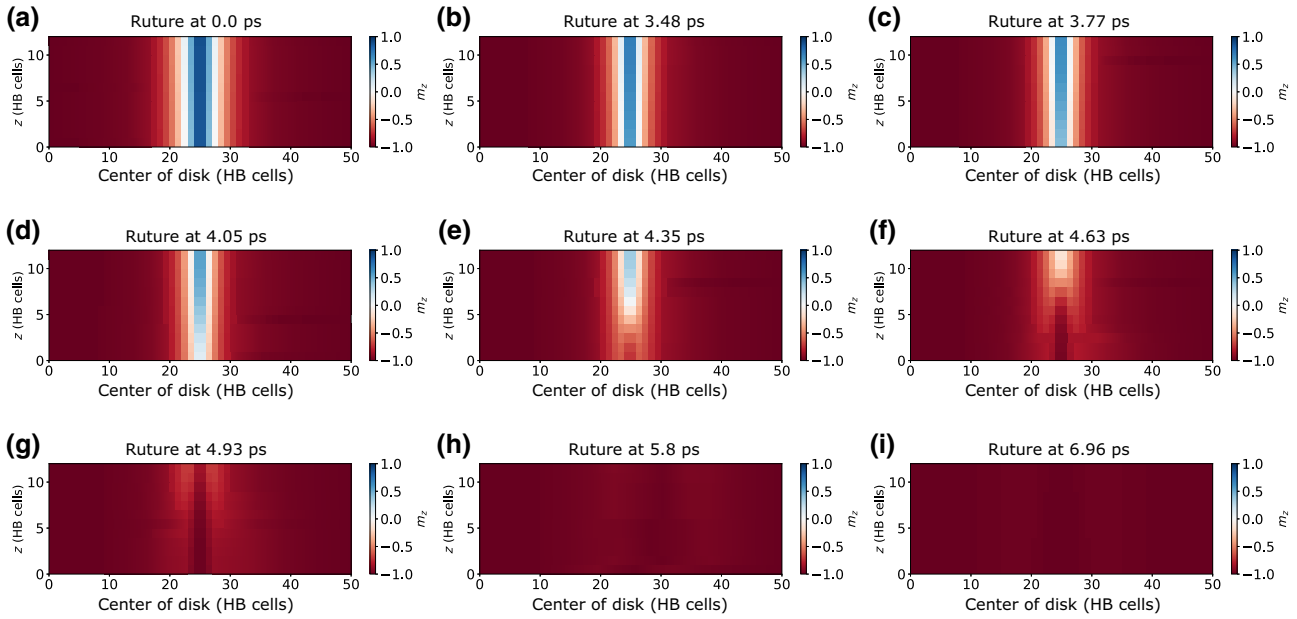

FIG. 4. The rupture process in detail in a side view of the disk: the skyrmion core, as visible in (a), switches its directions on the order of femtoseconds, generating a Bloch point that travels through the sample [(d)–(f)] to enable the skyrmion-core reversal. The previous skyrmion domain wall still exists after the reversal and the system then transforms into the uniform state. The simulation is counted from a point in time shortly before the reversal occurs.

Figure 5(b) shows that the rupture field decreases (linearly) with increasing values of the anisotropy strength K_u. For small K_u, one is closer to the spin-reorientation transition: this stabilizes the skyrmion DW, since in-plane configurations are more favorable compared to systems with high anisotropy, leading to a lower energy of the skyrmion state in comparison to the uniformly magnetized configuration. The energy of the FM state decreases since the absolute value of E_{ani} decreases with increasing anisotropy strength. A similar linearity is also given in the simpler Stoner-Wolfarth (SW) model [42]. The model describes a hysteretic behavior of single-domain ferromagnets, while the coercive field H_C of the systems scales linearly with the anisotropy constant, $H_C = 2K/M_S$. The coercive field in the SW model is the field strength at which a sample shows zero net magnetization. While H_C increases with K, we see a linear decrease of H_{rup} with the anisotropy.

Figure 5(c) shows the DMI-strength dependence of H_{rup}, which increases for higher D. The DMI stabilizes chiral spin structures and favors the skyrmion state compared to the FM state. The energy of the skyrmion state shrinks, resulting in a higher energy barrier, assuming a scaling of the barrier between the FM and the skyrmion state. The energy of the FM state should increase with higher D, since the parallel alignment does not minimize E_{DMI}. The results are thus in agreement with previous publications [12,36] for skyrmion rupture. H_{rup} increases with D in the whole range of (meta)stable skyrmions.

Figure 5(d) shows data for the influence of M_S on the annihilation field. Due to stronger dipolar interactions between the skyrmion core and the ring, with opposite magnetization surrounding the skyrmion, a higher M_S stabilizes the skyrmion. A stronger stray field should increase the energy of the FM state due to the stronger far field of this configuration. The combined effect can lead to an increasing H_{rup} for larger M_S.

We repeat the simulations for a smaller disk size ($d_{\text{disk}} = 120$ nm instead of $d_{\text{disk}} = 160$ nm). The resulting data for the rupture field are also displayed in each subplot of Fig. 5. The qualitative behavior is the same as for the disk with $d_{\text{disk}} = 160$ nm. Quantitatively, the values are up to a few percent lower. Those changes are small, although the area of the disk decreases by nearly a half, reducing, for example, the stabilizing stray field. Our interpretation is that the annihilation of the small skyrmion is the dominating factor in the process. For this, it does not matter very much how large the disk is.

C. Limit of the micromagnetic model

The dependence of the annihilation field H_{rup} on single magnetic parameters is shown in more detail in Fig. 5. To underline the importance of the simulation model, we perform the described simulations above in a purely micromagnetic model with different lateral cell sizes ($a_l = 2$ nm and $a_l = 1$ nm), and also in a full Heisenberg model, and using the multiscale model (see Sec. II).

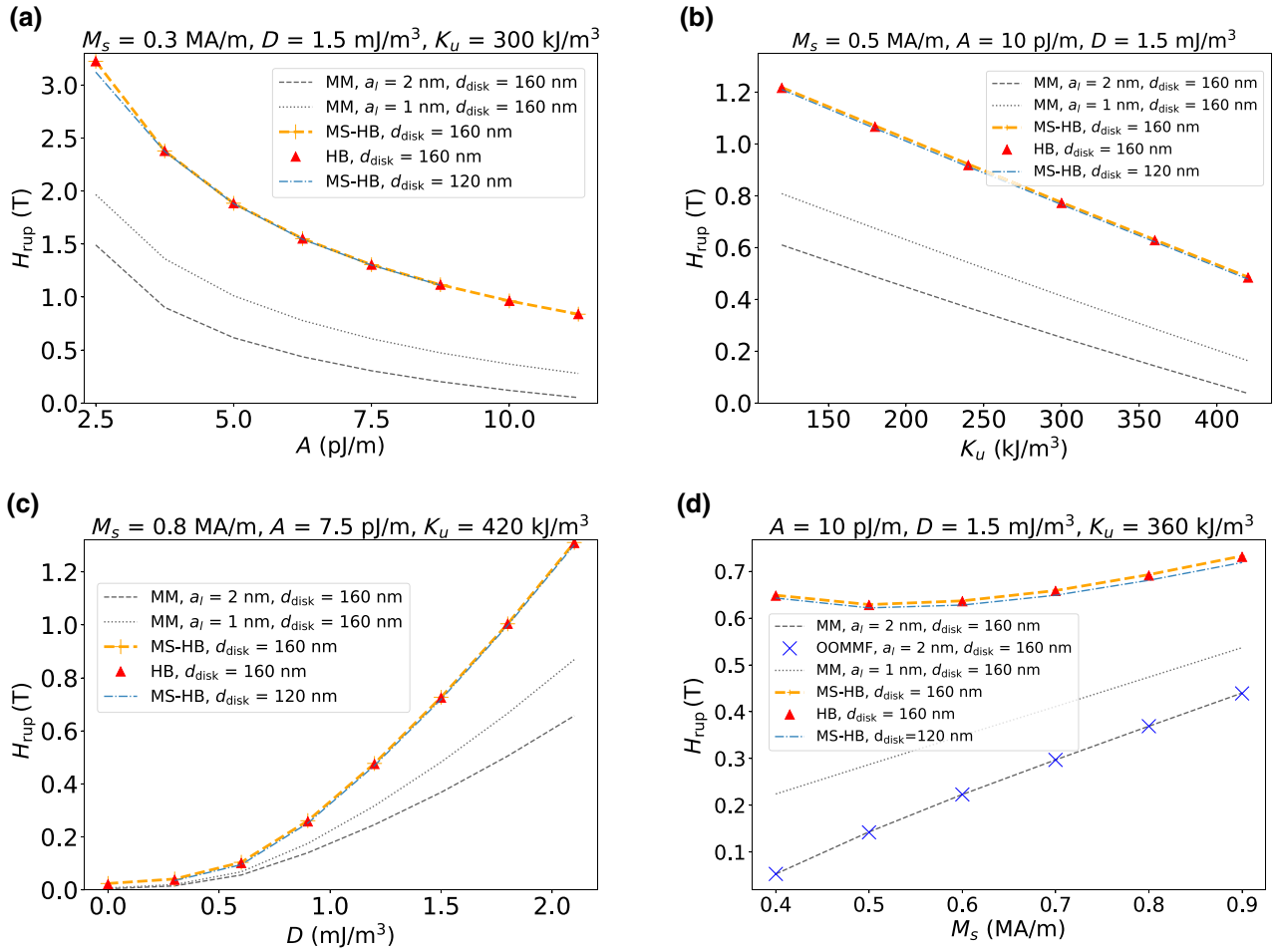

FIG. 5. The rupture field H_{rup} as a function of different magnetic parameters, studied with different computational models, for two geometries. The most important data points are from the Heisenberg (HB) model (red) and the multiscale with Heisenberg (MS) region (yellow). We consider the HB data to be the most accurate data and the MS data to be a computationally efficient approximation. The two data sets are practically identical and we describe them first and then, additionally, comment on the other lines shown: (a) the rupture field H_{rup} decreases with increasing exchange stiffness A; (b) H_{rup} decreases linearly with the anisotropy constant K_u; (c) H_{rup} increases as a function of the DMI strength D; and (d) H_{rup}, as a function of the saturation magnetization M_S, is roughly constant up to $M_s = 0.6$ MA/m and then increases for larger M_s. The two black lines show results computed using the micromagnetic (MM) model (black) for a discretization cell size of 1 nm (dotted) and 2 nm (dashed). The micromagnetic model results should be independent of the chosen discretization length: as this is not the case, the main observation is that the micromagnetic model does not accurately describe the rupture process. The blue crosses in (d) show results computed with OOMMF. This is evidence that our micromagnetic model agrees with the OOMMF micromagnetic model as benchmark. All of the data discussed above are for a disk diameter of 160 nm. In addition, the thin blue line shows multiscale-model results for a diameter of 120 nm, to give an indication of the sensitivity of H_{rup} to the geometry.

The data based on the MM model in Fig. 5 deviate very substantially from the HB-model results. This shows that MM simulations with the chosen cell size (which is typical for micromagnetic studies) can lead to inaccurate results.

We repeat the micromagnetic simulations carried out using MicroMagnum with the Object-Oriented MicroMagnetic Framework (OOMMF) [43], which is driven through the ubermag framework [44]. One set of results is shown in Fig. 5(d) and agrees with the results obtained using MicroMagnum. This is evidence that the observed deviation between the Heisenberg and micromagnetic models originates from the micromagnetic model rather than our MicroMagnum implementation of it.

We conclude that very small skyrmions, as they occur in the annihilation process based on the shrinking of the skyrmion, can no longer be resolved in a coarse mesh as used for micromagnetics. Figure 6(a) shows the skyrmion size in the HB (on the left) and the MM model (on the right) within the same subplot. The x axis represents a spatial coordinate of a scan through the disk, where for positions < 200, data from the Heisenberg model are used and for positions > 200, data from the micromagnetic

model are used. The y axis correlates with the changing external field. The width of the blue region in the x direction corresponds to the size of the skyrmion core. We see in Fig. 6(a) that the skyrmion size is in both models very similar, as long as the MM model is able to host the skyrmion. The pure HB model gives the most accurate result and is able to resolve a much smaller skyrmion (on the left) than the micromagnetic model (on the right) can do. It is therefore not surprising that the micromagnetic description of the annihilation process—which involves the shrinking and then annihilation of the skyrmion via a topological rupture—depends strongly on the chosen discretization when computed with the micromagnetic model and is thus inaccurate. Alternative computational models include the HB model, which is computationally too expensive. The multiscale model, which combines the Heisenberg model and the micromagnetic model, is a compromise that provides good accuracy where necessary and good performance through use of the micromagnetic model where possible.

In Fig. 5, we compare results computed using the MS model and the HB model. We find that the multiscale model overestimates the rupture field by only 1-2 mT, which is just above the chosen field step size of 1 mT. The small overestimation might come from the overestimation of the stray field due to the exclusive MM part of the sample: since there is no discretization in the z direction, the stray field might be higher than in a calculation performed in the full HB model, where spins can tilt at the surface due to demagnetization effects. However, the MS approach is not limited to any discretization of the MM mesh, also allowing for discretization in the z direction. The chosen discretization, however, shows sufficient accuracy for our purpose. Thus, the MS approach can provide a fast and robust evaluation of spin dynamics in larger samples, where HB calculations are not feasible.

We also want to discuss briefly the effect of temperature on the simulation results. In general, thermal noise should lower the annihilation fields, since the random fluctuations allow the system to reach energetically higher states. However, increasing the temperature of a sample can also vary the magnetic parameters drastically [45]. We expect this effect to have a much higher influence on the annihilation field, since varying those parameters may change H_{rup} by some factors, as can be seen in Fig. 5. While the HB model is able to simulate temperature effects accurately, the MM model has only restricted possibilities to simulate those effects, since the cell discretization leads to a cutoff of the spin-wave spectrum at wavelengths on the order of the cell size. It might be challenging to include thermal effects in the multiscale model, since the wave spectra at the interface need to be treated in a way that minimizes errors in the cross-scale embedding.

D. Expulsion field of skyrmions

Starting from the initial skyrmion states obtained at zero applied field (see Sec. A), we now investigate the process of annihilating the skyrmion by applying an external field in the positive z direction (we discuss the application of the field in the negative z direction in Sec. B).

In the context of the initial skyrmion configuration as represented in Fig. 2(d), we apply the external field in the positive z direction, which is the direction of the skyrmion core. The core will grow in response to the applied field because this will reduce the Zeeman energy of the system. When the skyrmion core has expanded so far that the helix of the skyrmion approaches the boundary of the disk, the

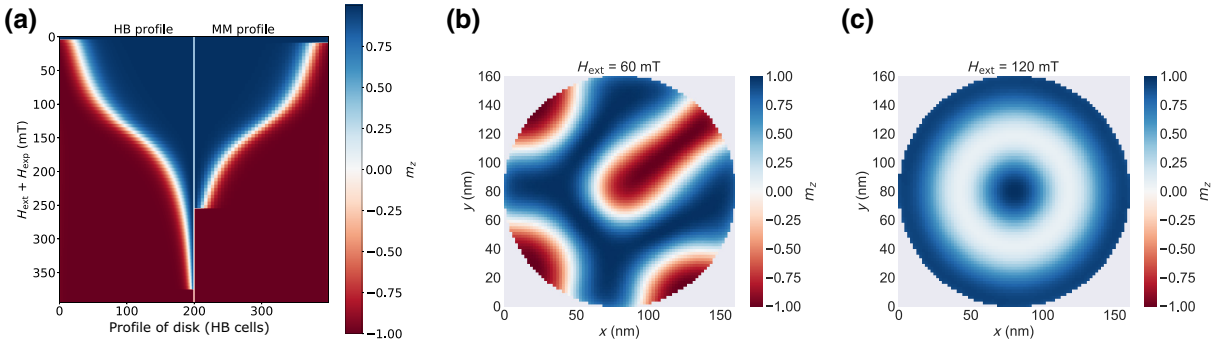

FIG. 6. (a) The dependence of the skyrmion profile on the field and the computational model. The x axis represents a line scan through the disk in the diametric direction, with the skyrmion core at the center (at position 200). The color shows the z component of the magnetization. The left side of the plot (up to HB cell 200) is taken from a Heisenberg model (with an lateral magnetic moment spacing of 0.4 nm), whereas the right (HB cell 201 and larger) is taken from the micromagnetic model calculations with a 2 nm lateral cell size. (b) The transition state during the expulsion of the simulation point in Fig. 7(b), for $K_u = 120$ MJ/m^3. The skyrmion is not directly expelled but undergoes a transition into a spin spiral state. (c) The transition state during the expulsion of the simulation point in Fig. 7(d), for $M_S = 0.9$ MA/m. The skyrmion is not directly expelled but undergoes a transition into a target configuration without a negative m_z-component.

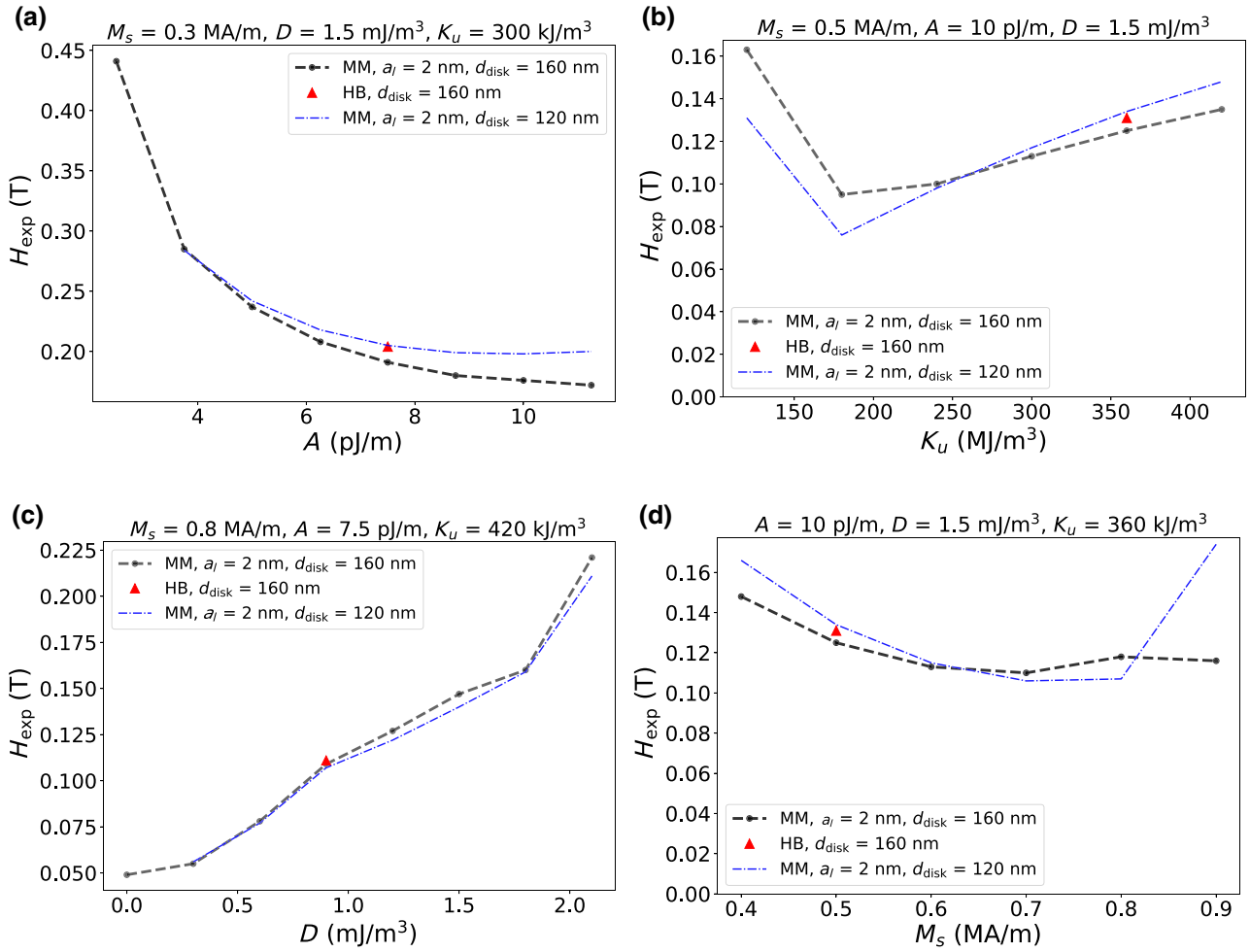

FIG. 7. The expulsion field H_{exp} as a function of different magnetic parameters. The HB, multiscale, and micromagnetic simulations are in very good agreement for the data shown here and only the micromagnetic data are shown. The gray lines indicate the transition into nonskyrmionic states for the usual disk diameter. The dependence of the expulsion field H_{exp} is shown as a function of (a) the exchange stiffness A, (b) the anisotropy constant K_u, (c) the DMI strength D, and (d) the saturation magnetization M_S.

magnetization helix can unwind at the boundary (without rupturing the continuous magnetization vector field).

Figures 2(d)–2(f) show the process of expulsion. In this scenario, we call the annihilation field the *expulsion* field $H_{exp} = H^*$.

We define H_{exp} as the lowest field value at which no magnetization component is pointing against the field direction, which means when $\min(m_z) \geq 0$. During simulation of the field application, some of the intermediate magnetic configurations may not be skyrmion configurations but more complex spin spiral structures.

Figure 7 shows the dependence of H_{exp} on different magnetic parameters. In contrast to the application of the field in the opposite direction—and the associated skyrmion annihilation through skyrmion shrinking and rupture, the expulsion process is within the domain of applicability of the micromagnetic model and thus the Heisenberg and the micromagnetic model provide very comparable results (and there is no need to use the multiscale model). Here, we discuss the results of the micromagnetic approach. Figure 7(a) shows the dependence of the expulsion field as a function of the exchange coupling. Similar to the rupture process in Fig. 5(a), a strong exchange lowers H_{exp}, as the uniform configuration becomes energetically more attractive than the skyrmion with increasing exchange coupling. Although the skyrmion radius is smaller for a stronger exchange constant A at zero field [see, e.g., Fig. 3(a)], the skyrmion increases in size much faster with an increasing field, leading to expulsion at the disk boundary at lower fields. In Fig. 7(b), an approximately linear dependence of H_{exp} for K_u is observed over a wide range of anisotropy strengths. A strong anisotropy avoids large IP components and thus tries to prevent the IP skyrmion DW for a strong size increase with increased field strengths. Such linear behavior is also observed for H_{rup}. However, one outlier for $K_u = 120$ MJ/m^3 is observed. This

configuration has a transition into a spin spiral state during the field ramping, which leads to the discontinuous behavior. The configuration is also shown in Fig. 6(b).

As seen in Fig. 7(c), for the DMI we find an increase in H_{exp} for stronger D, similar to the rupture. A skyrmion configuration reduces the DMI energy in the system with high D; similarly, the energy of the FM state increases, also increasing the barrier between the states. For strong DMI, H_{exp} is therefore higher.

As is visible in Fig. 7(d), the dependence of H_{exp} on M_S shows a dip for intermediate values, rising slowly again for $M_S = 0.8$ MA/m. For this value, the system is close to the spin-reorientation transition, when the system loses perpendicular magnetic anisotropy and favors IP magnetization. In Fig. 7(d), a special case is the point for 160-nm disk size and $M_S = 0.9$ MA/m. Here, a target configuration evolves without negative z component [see Fig. 6(c)], reaching the criterion for the chosen definition of H_{exp}. For the smaller disk size, the qualitative behavior is the same, except for an outlier for large M_S, where the magnetic state transitions into a nonskyrmionic configuration with a large IP component.

Changing the disk size affects the expulsion process more strongly than the rupture process. We find a maximum change of around 25% when comparing the expulsion field for the disk with a 120-nm diameter to the one with a 160-nm diameter (neglecting the discussed special cases with complex transition states). The expulsion is not a localized process and thus depends strongly on the sample geometry and the skyrmion size dependence on the field. For different parameter sets, H_{exp} might increase or decrease. Figure 8 shows two different skyrmion diameters for two parameter sets from Fig. 7(b). Figure 8(a) shows the case where the smaller disk has a lower H_{exp}, Fig. 8(b) shows the case where the smaller disk has a higher H_{exp}. The first case shows stray-field stabilized skyrmions also at zero field. Both skyrmions increase their size approximately linearly, while the larger disk size allows for a larger size before the expulsion takes place. In the latter case—DMI-stabilized skyrmions at zero field—we see a large sudden increase of the skyrmion size at around 50 mT, which is the transition from the DMI stabilization to a stray-field stabilization [19]. In that case, the jump is less distinct for the smaller disk, caused by less stray field in a smaller sample. Due to this effect, the relative size of the skyrmion in the stray-field-stabilized regime is smaller for the disk with $d = 120$ nm and the following linear increase due to the field stabilizes a skyrmion at higher fields than in the large disk. This leads to different trends of H_{exp} by changing disk sizes.

For the expulsion process, there is no need to use a HB model, since no BP or other strong spin canting occurs that would require a more accurate model. Small deviations between the HB and the MM model may originate from discretization errors, since the chosen finite-difference method [46] approximates the circular disk by a rectangular mesh.

We also find that for most parameter sets, H_{exp} is in general around one order of magnitude smaller than H_{rup}, since the topological charge does not protect the spin structure against expulsion.

V. CONCLUSION

We investigated the process of the transition from a skyrmion in a disk geometry to a uniformly magnetized state using an external magnetic field that is applied in

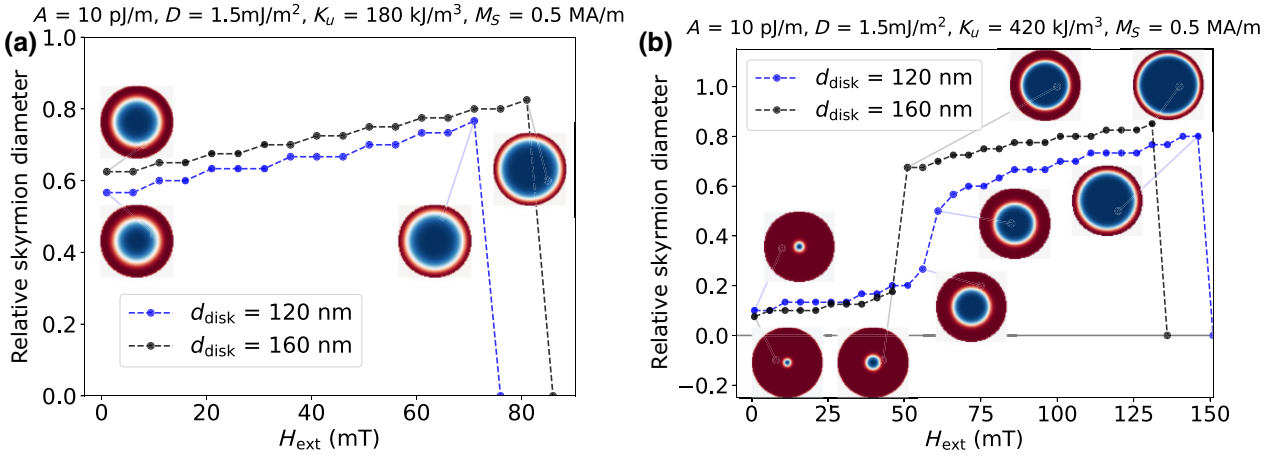

FIG. 8. The skyrmion radius for selected parameter sets from Fig. 7(b) for different disk sizes. The insets show the magnetic configuration at the respective field. It is clearly visible that small skyrmions at lower fields show a large step during the transition from DMI stabilization to stray-field stabilization [in (b), at around 50 mT]. This jump is considerably smaller for smaller disk sizes due to smaller stray fields in that sample, which then result in a higher expulsion field. If the skyrmions are strayfield-stabilized at zero-field, there is no sudden size increase and larger disk sizes show the larger expulsion field (a).

the out-of-plane direction. We find two different reversal mechanisms, depending on the direction of the applied field relative to the direction of the magnetization in the skyrmion core.

If the direction of the magnetization in the core of the skyrmion points in the same direction as the applied field, then the skyrmion core will grow with an increasing field, until the whole disk is uniformly magnetized in the direction of the applied field. The skyrmion in this expulsion process is driven out of the sample by growing the core and the skyrmion domain wall unwinding at the circumferential boundary of the disk geometry.

If the direction of the applied field points in the opposite direction of the magnetization in the corner, then the skyrmion core shrinks with increasing external field strength, until the field is sufficiently strong to remove the skyrmion from the sample. In the process, a rupture of the magnetization vector field occurs, to allow for the skyrmion to be annihilated at the center of the disk. The microscopic annihilation mechanism is facilitated by a Bloch point moving through the thickness of the sample, which reverses the direction of the core.

For both directions, we determine the required strength of the applied field that is required to annihilate the skyrmion from the sample, which we refer to as the expulsion field or the rupture field, depending on the mechanism of annihilation of the skyrmion.

We show that the rupture field H_{rup} of skyrmions in a confined geometry depends strongly on the material parameters, while the dependence on the disk size is rather small in the observed regime of around 100 nm. The independence from the disk-size relates to the annihilation of the skyrmion taking place in the center of the disk as a local process, for which the total size of the disk is not important. The disk size plays a large role for the expulsion process though, as the skyrmion core grows until it reaches the boundary of the disk. We find that the skyrmion expulsion field H_{exp} is in general one order of magnitude smaller than H_{rup}, since no highly energetic BP occurs during the annihilation of the topological charge.

For the potential use of skyrmions in a data-storage device, the skyrmion lifetime has to be chosen in such a way that, on the one hand, imprinting a state is possible and energy efficient but, on the other, data retention has to be ensured over the device lifetime (or at least a reasonable time span) in the presence of thermal fluctuations. The energy barrier, probed indirectly by our investigations, is the main parameter used to adjust this trade-off. One important outcome of these investigations is that it is easier to annihilate the skyrmion state without generating a BP. This result is consistent with other studies, where a smaller energy barrier has been found for skyrmions to disappear via a sample boundary rather than through shrinking [12].

With skyrmions in confined geometries one could imagine designing a BPM storage device [15], which is able to store more than one bit in one geometry: at least four states are imaginable as metastable states for the disks (skyrmion up, uniform up, skyrmion down, uniform down). This would lead to a potentially very significant increase of the storage capacity for such devices: with n binary storage units (i.e., bits), one can encode 2^n states, whereas with n storage units of this base 4, the number of storable bits doubles for the same amount of bit patterns.

We use two different simulation models, a Heisenberg model and a micromagnetic model. We find that the micromagnetic model cannot accurately resolve the annihilation process due to BP formations: the computed behavior depends on the micromagnetic cell size which, however, should not affect the observed physics in a reliable simulation. In the rupture process, the skyrmion core shrinks down to one line of magnetic moments, which cannot be resolved in the micromagnetic representation.

In all other simulations, we find close agreement between the Heisenberg model and the micromagnetic model. Where the micromagnetic model cannot be used but the Heisenberg model is computationally too expensive to employ, a multiscale model is used successfully, which represents the sample in the Heisenberg model where necessary and in the micromagnetic model where possible.

ACKNOWLEDGMENTS

Thomas Winkler and the group in Mainz acknowledge funding from the Emergent AI Center, funded by the Carl-Zeiss-Stiftung, the German Research Foundation (DFG SFB TRB 173, SPIN+X, A01 403502522; SPP Skyrmionics), and the European Research Council (ERC-2019-SyG, 3D MaGiC, ID: Grant No. 856538). This work was also financially supported by the Engineering and Physical Sciences Research Council's United Kingdom Skyrmion Project Grant (Grant No. EP/N032128/1). We further acknowledge fruitful discussions with Ulrich Nowak, Oleg Tretiakov, and Karin Everschor-Sitte.

APPENDIX

To corroborate the robustness of our results, the HB code of MicroMagnum is checked with simulation software developed by Markus Weiäenhofer [47,48]. The resulting annihilation field of a skyrmion configuration ($c_s = 4$, $a = 0.4$ nm, $M_s = 0.5$ MA/m $\times\, a^3$, $J = 3$ pJ $\times\, a/n_{\mathrm{nn}}$, $D = 3$ mJ/m^2 $\times\, a^2/n_{\mathrm{nn}}$ and $K_u = 480$ kJ/m^3 $\times\, a^3$, the sample was 16 nm $\times$ 16 nm) is in very good agreement (HB simulation in MicroMagnum $H_{\mathrm{rup}} = 3.62$ T, compared to $H_{\mathrm{rup}} = 3.625$ T, deviation below 0.15%). For a more general validation of the HB approach of MicroMagnum, see Ref. [24].

To exclude simulation artifacts due to a lack of symmetry breaking in the finite-difference-method simulations, the OOP H_{rup} is determined, by simultaneously applying a

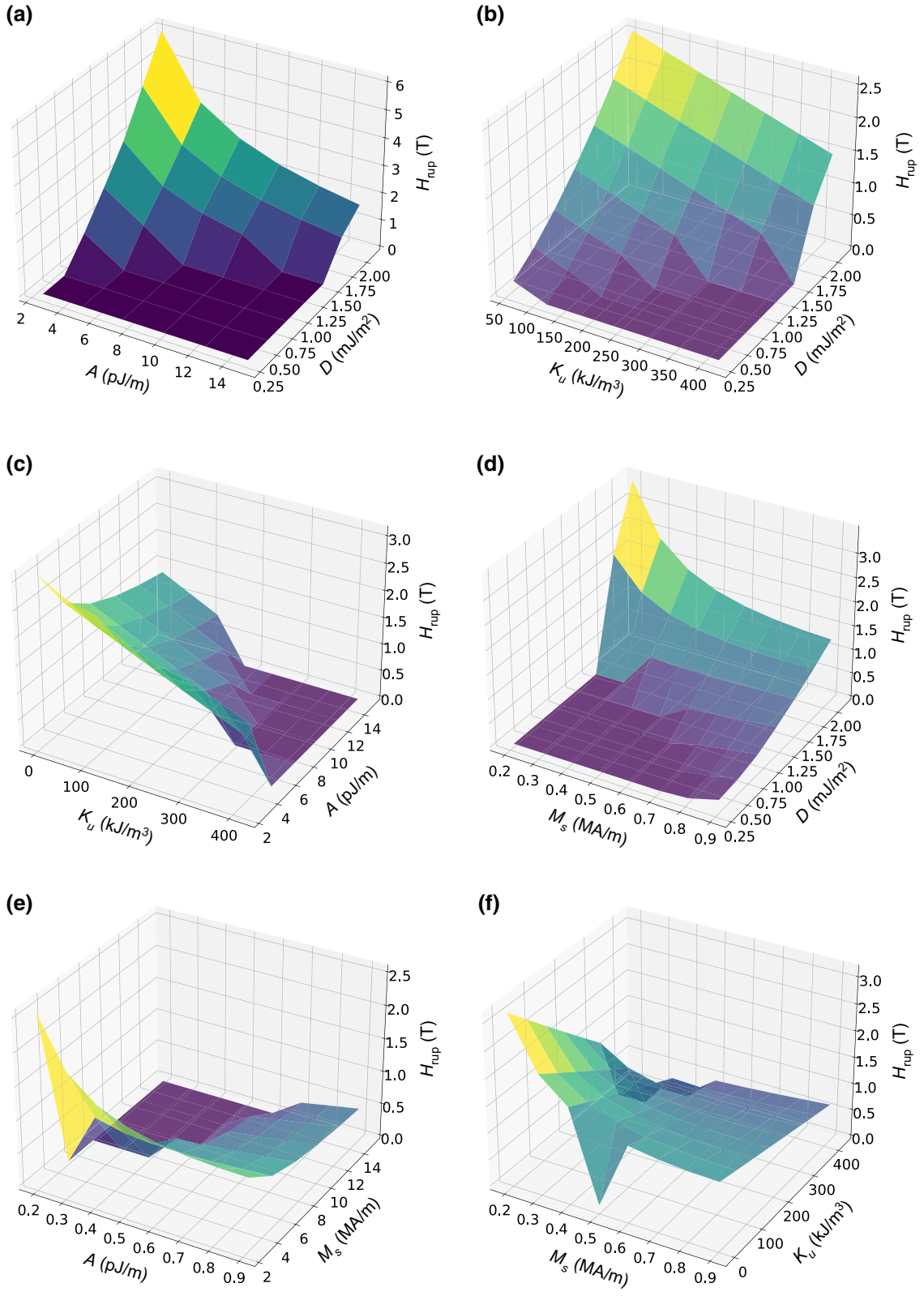

FIG. 9. The rupture field H_{rup} as a function of different magnetic parameters, evaluated in the MS model. The same parameter sets as in Fig. 3 are used. If the configuration is a nonskyrmion configuration, H_{rup} describes the field when the system is homogeneously OOP magnetized. For a detailed discussion on the dependence of every parameter, see Sec. IV B.

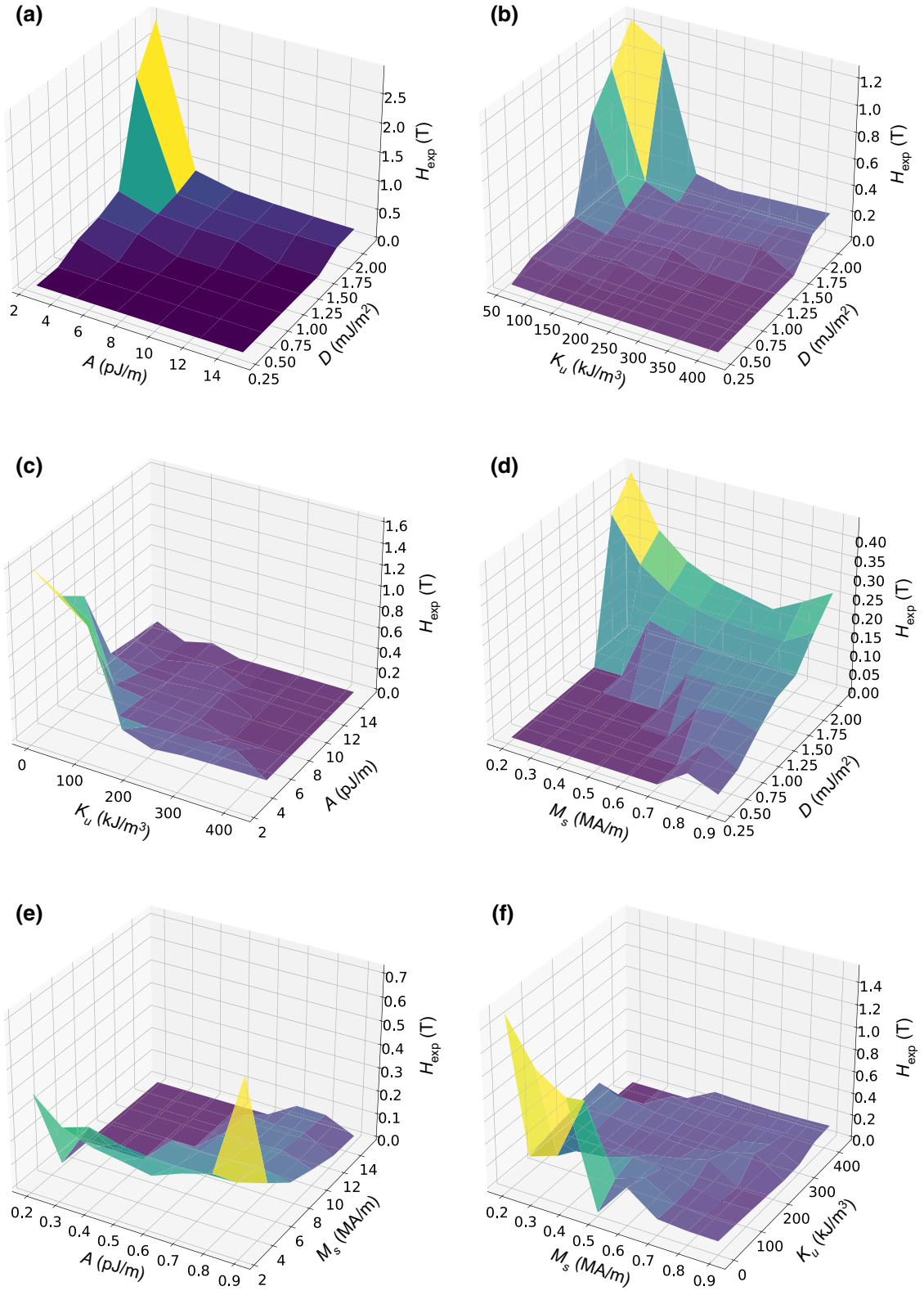

FIG. 10. The expulsion field H_{exp} as a function of different magnetic parameters, evaluated by an MM model with 2 nm lateral cell size. The same parameter sets as in Fig. 3 are used. If the configuration is a nonskyrmion configuration, H_{exp} describes the field when there is no magnetization component in the $-z$ direction. For a detailed discussion on the dependence of every parameter, see Sec. IV D. Due to transitions into various magnetic configurations, the dependence is not always as continuous as for the rupture.

small constant IP field, not aligned with any of the simulation grid axes. The simulations show that the annihilation field does not vary for small IP fields of several tens of millitesla. This is an indicator that our simulations are not dominated by a lack of symmetry breaking, as could occur due to the highly symmetric simulation.

Figures 9 and 10 show the rupture field and expulsion field, respectively, for all parameter sets presented in Fig. 3.

[1] K. Everschor-Sitte, J. Masell, R. M. Reeve, and M. Kläui, Perspective: Magnetic skyrmions—overview of recent progress in an active research field, J. Appl. Phys. **124**, 240901 (2018).

[2] Y. Tokura and N. Kanazawa, Magnetic skyrmion materials, Chem. Rev. **121**, 2857 (2021), PMID: 33164494.

[3] I. Dzyaloshinsky, A thermodynamic theory of "weak" ferromagnetism of antiferromagnetics, J. Phys. Chem. Solids **4**, 241 (1958).

[4] T. Moriya, Anisotropic superexchange interaction and weak ferromagnetism, Phys. Rev. **120**, 91 (1960).

[5] D. Pinna, F. A. Araujo, J.-V. Kim, V. Cros, D. Querlioz, P. Bessière, J. Droulez, and J. Grollier, Skyrmion Gas Manipulation for Probabilistic Computing, Phys. Rev. Appl. **9**, 064018 (2018).

[6] J. Zázvorka, F. Jakobs, D. Heinze, N. Keil, S. Kromin, S. Jaiswal, K. Litzius, G. Jakob, P. Virnau, and D. Pinna *et al.*, Thermal skyrmion diffusion used in a reshuffler device, Nat. Nanotechnol. **14**, 658 (2019).

[7] R. Tomasello, E. Martinez, R. Zivieri, L. Torres, M. Carpentieri, and G. Finocchio, A strategy for the design of skyrmion racetrack memories, Sci. Rep. **4**, 6784 (2014).

[8] A. Fert, V. Cros, and J. Sampaio, Skyrmions on the track, Nat. Nanotechnol. **8**, 152 (2013).

[9] F. Büttner, I. Lemesh, M. Schneider, B. Pfau, C. M. Günther, P. Hessing, J. Geilhufe, L. Caretta, D. Engel, and B. Krüger *et al.*, Field-free deterministic ultrafast creation of magnetic skyrmions by spin-orbit torques, Nat. Nanotechnol. **12**, 1040 (2014).

[10] S. Finizio, K. Zeissler, S. Wintz, S. Mayr, T. Weßels, A. J. Huxtable, G. Burnell, C. H. Marrows, and J. Raabe, "Deterministic field-free skyrmion nucleation at a nanoengineered injector device, Nano Lett. **19**, 7246 (2019).

[11] S. Woo, K. M. Song, X. Zhang, M. Ezawa, Y. Zhou, X. Liu, M. Weigand, S. Finizio, J. Raabe, and M.-C. Park *et al.*, Deterministic creation and deletion of a single magnetic skyrmion observed by direct time-resolved x-ray microscopy, Nat. Electron. **1**, 288 (2018).

[12] D. Cortés-Ortuño, W. Wang, M. Beg, R. A. Pepper, M.-A. Bisotti, R. Carey, M. Vousden, T. Kluyver, O. Hovorka, and H. Fangohr, Thermal stability and topological protection of skyrmions in nanotracks, Sci. Rep. **7**, 1 (2017).

[13] S. Woo, K. Litzius, B. Krüger, M.-Y. Im, L. Caretta, K. Richter, M. Mann, A. Krone, R. M. Reeve, and M. Weigand *et al.*, Observation of room-temperature magnetic skyrmions and their current-driven dynamics in ultrathin metallic ferromagnets, Nat. Mater. **15**, 501 (2016).

[14] K. Litzius, I. Lemesh, B. Krüger, P. Bassirian, L. Caretta, K. Richter, F. Büttner, K. Sato, O. A. Tretiakov, and J. Förster *et al.*, Skyrmion Hall effect revealed by direct time-resolved x-ray microscopy, Nat. Phys. **13**, 170 (2017).

[15] H. Richter, A. Dobin, O. Heinonen, K. Gao, R. vd Veerdonk, R. Lynch, J. Xue, D. Weller, P. Asselin, and M. Erden *et al.*, Recording on bit-patterned media at densities of 1 Tb/in^2 and beyond, IEEE Trans. Magn. **42**, 2255 (2006).

[16] S. H. Charap, P.-L. Lu, and Y. He, Thermal stability of recorded information at high densities, IEEE Trans. Magn. **33**, 978 (1997).

[17] B. Göbel and I. Mertig, Skyrmion ratchet propagation: Utilizing the skyrmion Hall effect in ac racetrack storage devices, Sci. Rep. **11**, 1 (2021).

[18] J. Zázvorka, F. Dittrich, Y. Ge, N. Kerber, K. Raab, T. Winkler, K. Litzius, M. Veis, P. Virnau, and M. Kläui, Skyrmion lattice phases in thin film multilayer, Adv. Funct. Mater. **30**, 2004037 (2020).

[19] F. Büttner, I. Lemesh, and G. S. Beach, Theory of isolated magnetic skyrmions: From fundamentals to room temperature applications, Sci. Rep. **8**, 1 (2018).

[20] L. Desplat, C. Vogler, J.-V. Kim, R. Stamps, and D. Suess, Path sampling for lifetimes of metastable magnetic skyrmions and direct comparison with Kramers' method, Phys. Rev. B **101**, 060403 (2020).

[21] R. Zivieri and O. Chubykalo-Fesenko, in *Magnetic Skyrmions and Their Applications*, (Elsevier, 2021), p. 181.

[22] W. F. Brown Jr, Thermal fluctuations of a single-domain particle, Phys. Rev. **130**, 1677 (1963).

[23] E. Feldtkeller, Mikromagnetisch stetige und unstetige Magnetisierungskonfigurationen, Zeitschrift fur Angewandte Physik **19**, 530–+ (1965).

[24] A. De Lucia, B. Krüger, O. A. Tretiakov, and M. Kläui, Multiscale model approach for magnetization dynamics simulations, Phys. Rev. B **94**, 184415 (2016).

[25] D. Hinzke and U. Nowak, Monte Carlo simulation of magnetization switching in a Heisenberg model for small ferromagnetic particles, Comput. Phys. Commun. **121**, 334 (1999).

[26] S. Blundell, Magnetism in condensed matter (2003).

[27] T. Lancaster and S. J. Blundell, *Quantum Field Theory for the Gifted Amateur* (Oxford University Press, Oxford, 2014).

[28] C. Abert, L. Exl, G. Selke, A. Drews, and T. Schrefl, Numerical methods for the stray-field calculation: A comparison of recently developed algorithms, J. Magn. Magn. Mater. **326**, 176 (2013).

[29] A. J. Newell, W. Williams, and D. J. Dunlop, A generalization of the demagnetizing tensor for nonuniform magnetization, J. Geophys. Res.: Solid Earth **98**, 9551 (1993).

[30] A. Drews, G. Selke, and B. Krueger *et al.*, MicroMagnum github repository, https://github.com/micromagnum/micromagnum, (2014).

[31] G. Selke, Ph.D. thesis, University of Hamburg, 2013.

[32] K. Litzius, Ph.D. thesis, Johannes Gutenberg Universität Mainz, Germany, 2018.

[33] T. B. Winkler, Master's thesis, Johannes Gutenberg Universität Mainz, Germany, 2018.

[34] A. V. Ivanov, D. Dagbartsson, J. Tranchida, V. M. Uzdin, and H. Jónsson, Efficient optimization method for finding minimum energy paths of magnetic transitions, J. Phys.: Condens. Matter **32**, 345901 (2020).

[35] S. Emori, U. Bauer, S.-M. Ahn, E. Martinez, and G. S. Beach, Current-driven dynamics of chiral ferromagnetic domain walls, Nat. Mater. **12**, 611 (2013).

[36] A. De Lucia, K. Litzius, B. Krüger, O. A. Tretiakov, and M. Kläui, Multiscale simulations of topological transformations in magnetic-skyrmion spin structures, Phys. Rev. B **96**, 020405 (2017).

[37] M. Beg, R. Carey, W. Wang, D. Cortés-Ortuño, M. Vousden, M.-A. Bisotti, M. Albert, D. Chernyshenko, O. Hovorka, and R. L. Stamps *et al.*, Ground state search, hysteretic behaviour and reversal mechanism of skyrmionic textures in confined helimagnetic nanostructures, Sci. Rep. **5**, 1 (2015).

[38] W. Akhtar, A. Hrabec, S. Chouaieb, A. Haykal, I. Gross, M. Belmeguenai, M. Gabor, B. Shields, P. Maletinsky, and A. Thiaville *et al.*, Current-Induced Nucleation and Dynamics of Skyrmions in a Co-Based Heusler Alloy, Phys. Rev. Appl. **11**, 034066 (2019).

[39] U. Gradmann and J. Müller, Flat ferromagnetic, epitaxial ^{48}Ni/^{52}Fe(111) films of few atomic layers, Phys. Status Solidi (b) **27**, 313 (1968).

[40] C. Chui, F. Ma, and Y. Zhou, Geometrical and physical conditions for skyrmion stability in a nanowire, AIP Adv. **5**, 047141 (2015).

[41] A. Thiaville, S. Rohart, É. Jué, V. Cros, and A. Fert, Dynamics of Dzyaloshinskii domain walls in ultrathin magnetic films, EPL (Europhysics Letters) **100**, 57002 (2012).

[42] E. C. Stoner and E. Wohlfarth, A mechanism of magnetic hysteresis in heterogeneous alloys, Philos. Trans. R. Soc. London. Ser. A, Math. Phys. Sci. **240**, 599 (1948).

[43] M. Donahue, OOMMF *User's Guide, Version 1.0* (U.S. Department of Commerce, National Institute of Standards and Technology, Gaithersburg, MD, 1999).

[44] M. Beg, R. A. Pepper, and H. Fangohr, User interfaces for computational science: A domain specific language for OOMMF embedded in PYTHON, AIP Adv. **7**, 056025 (2017).

[45] F. Pawlek, in *Magnetische Werkstoffe* (Springer, 1952), p. 289.

[46] J. E. Miltat and M. J. Donahue *et al.*, Numerical micromagnetics: Finite difference methods, Handbook Magn. Adv. Magn. Mater. **2**, 742 (2007).

[47] M. Weißenhofer and U. Nowak, Diffusion of skyrmions: The role of topology and anisotropy, New J. Phys. **22**, 103059 (2020).

[48] M. Weißenhofer and U. Nowak, Orientation-dependent current-induced motion of skyrmions with various topologies, Phys. Rev. B **99**, 224430 (2019).